

Diagnostic Features of EPR Spectra of Superoxide Intermediates on Catalytic Surfaces and Molecular Interpretation of Their g and A Tensors

Kamila Sobańska¹ · Aneta Krasowska¹ · Tomasz Mazur¹ · Katarzyna Podolska-Serafin¹ · Piotr Pietrzyk¹ · Zbigniew Sojka¹

Published online: 13 August 2015

© The Author(s) 2015. This article is published with open access at Springerlink.com

Abstract The use of electron paramagnetic resonance spectroscopy to study the superoxide intermediates, generated by end-on and side-on adsorption of the naturally abundant and ^{17}O -enriched dioxygen on catalytic surfaces is discussed. Basic mechanisms of O_2^- radical formation via a cationic redox mechanism, an anionic redox mechanism, and an electroprotic mechanism are illustrated with selected oxide-based systems of catalytic relevance. Representative experimental spectra of various complexities are analyzed and their diagnostic features have been identified and interpreted. The molecular nature of the g and A tensors of the electrostatic and covalent superoxide adducts is discussed in detail within the classic and density functional theory based approaches.

Keywords EPR · DFT · Oxygen activation · Superoxide · Catalysis · Surface · Electron transfer · Adsorption · Radicals · Spectra analysis

1 Introduction

Activation of molecular dioxygen is one of the central problems of oxidative chemistry with long record of extensive experimental and theoretical investigations [1]. The peculiar electronic and magnetic structure of O_2 is related to its triplet $^3\Sigma_g^-$ ground state with two orthogonal $\pi_g^*(2p)$ singly-

occupied molecular orbitals (α -SOMO). Despite its open-shell nature, dioxygen exhibits relatively low reactivity. This feature is related to the triplet-singlet spin barrier [2], which can be circumvented upon O_2 activation on catalytic surfaces via complex networks of redox processes until the terminal O^{2-} ion is formed [1, 3]. It involves a sequence of gradual reduction and dissociation steps including $\text{O}_{2(g)} \rightarrow \text{O}_{2(\text{surf})} \rightarrow \text{O}_{2(\text{surf})}^- \rightarrow \text{O}_{(\text{surf})}^- \rightarrow \text{O}_{2(\text{surf})}^{2-} \rightarrow \text{O}_{(\text{lattice})}^{2-}$, where various surface reactive oxygen species (ROS), from electron-poor (electrophilic) to electron-rich (nucleophilic), of distinctly different reactivity and proton affinity, may appear. All of them can be directly involved in heterogeneous oxidation of exogenous organic reactants depending on process conditions [1]. Thus, the catalytic role of the surface active sites is to provide oxygen in a specific activated state, which then permits preferable reaction pathways of lower activation energy to take place. In the particular case of the transition-metal oxide or metallozeolite catalysts, the variety of shapes and favorable orientations of the energetically accessible $3d$ orbitals together with the multiplicity of valence and spin states of surface transition-metal ions allow them to react with dioxygen effectively, without violating symmetry and spin conservation rules [4, 5]. Paramagnetic oxygen species can be located on the surface or within the bulk of the catalyst when zeolites or mesoporous materials are involved. Electron paramagnetic resonance (EPR) alone, or more frequently combined with other techniques, has been successfully used to study their location, structure, and catalytic reactivity [1, 6–8]. In the case of well resolved spectra, the high information content as compared to that obtained from other spectroscopies used in catalytic research helps to identify the active centers or intermediates and their structure and spatial arrangement. However, since most of the catalytic materials are polycrystalline and exhibit high surface area, the use of powders may generate some difficulties for EPR studies

✉ Piotr Pietrzyk
pietrzyk@chemia.uj.edu.pl

¹ Faculty of Chemistry, Jagiellonian University, ul. Ingardena 3, 30-060 Kraków, Poland

connected with overlapping signals and decreased spectral resolution.

Extensive experimental and theoretical studies have been performed to elucidate the heterogeneous activation process of dioxygen, starting from early stages of O_2^- formation until final incorporation of the resultant O^{2-} ions into the oxide lattice [1]. Unlike diamagnetic O_2^{2-} and O^{2-} anions, the O^- and O_2^- oxygen species are paramagnetic and may be observed directly by means of EPR spectroscopy [9–11]. These radicals, especially when isotopically enriched $^{17}\text{O}_2$ is used, exhibit characteristic spectra of high information content, which allows one to characterize their molecular structure, formation, thermal stability, and reactivity.

The superoxide anion, O_2^- , is a particularly important intermediate of the one-electron reduction of dioxygen, which occurs widely in nature [12, 13] and in homo/heterogeneous catalytic processes [14–16]. The first step in activation of a dioxygen molecule consists of electron transfer (ET) from metal to ligand (MLET) to form a metal-superoxo adducts. It is feasible owing to the low-lying β -LUMO states, which can accommodate additional electron (and spin) density due to high electronegativity of oxygen. Both side-on (η^2) and end-on (η^1) modes of O_2 coordination were observed. Further electron density transfer may be followed by O–O bond cleavage, leading eventually to the formation of high-valent metal-oxo cores ($4e^-$ reduction), exemplified by, e.g., intrazeolite $\{\text{FeO}\}^+$ dispersed in ZSM-5 [17].

Another catalytically important way of facile generation of the superoxide radicals involves hydrogen peroxide catalytic chemistry [18–21]. Specific electroprotic interaction of H_2O_2 with the catalyst surface determines the nature of the resultant ROS, among them O_2^- and OH^\bullet radicals and peroxo O_2^{2-} species can be easily generated by controlling pH of the solution along with the redox properties, crystallinity, and surface acidity of the catalyst [21]. Apart from heterogeneous activation of dioxygen in the context of catalytic reactions, a number of important pathways to formation of O_2^- radicals have been recognized [22], where the mentioned elementary steps (ET, electroprotic interactions) are involved. They include for instance O_2 reduction by photo-excited conduction band electrons in semiconductors [23], enzymatic processes involving for instance NADH oxidase and cytochrome bc_1 complex [24], reactions in liquid phase between selected ROS (for instance $^\bullet\text{OH}$ radicals with H_2O_2) during Fenton-type processes [25] or reductive activation of O_2 in bioinorganic complexes [26].

The adsorbed superoxide anion is usually identified on the basis of its g and ^{17}O A tensors. Nonetheless, unambiguous proof for its formation at the surface of a catalyst can be obtained by analysis of the hyperfine pattern from the

EPR spectra obtained with ^{17}O -enriched oxygen since the natural abundance of this isotope, having a nuclear spin of $I = 5/2$, is very low (0.038 %). Complete resolution of the hyperfine structure is necessary in order to calculate the distribution of the electron spin density within the adsorbed superoxide species. This is important from the viewpoint of the surface chemistry since the total spin density on O_2^- reflects the degree of electron transfer from the surface center to the adsorbed molecule.

In this paper we describe typical features of the EPR spectra of the superoxide $^{16}\text{O}_2^-$ and $^{17}\text{O}_2^-$ radicals stabilized on various catalytic surfaces, provide simple guidelines for their straightforward analysis and molecular interpretation of the extracted parameters. The classic semiempirical approaches are supplemented by density functional theory (DFT) calculations. A concise and non-technical sketch of the EPR spectra analysis of the surface superoxide species presented in this paper may be helpful for a broader audience interested in the practical aspects of EPR spectroscopy in this field, and discussion of the surveyed case studies.

2 Experimental Part

Selected examples of surface superoxide intermediates discussed in this paper include the following catalytic materials: $12\text{CaO} \cdot 7\text{Al}_2\text{O}_3$ calcium aluminate (mayenite), amorphous Nb_2O_5 and ZrO_2 oxides, transition-metal ion (TMI) exchanged ZSM-5 and dealuminated SiBEA zeolites, and TMI supported on SiO_2 . The polycrystalline mayenite samples were obtained by conventional high temperature solid-state reaction between analytical grade CaCO_3 (Aldrich) and $\gamma\text{-Al}_2\text{O}_3$ (Aldrich) as described elsewhere [27, 28]. Amorphous Nb_2O_5 and ZrO_2 oxides were prepared by hydrolysis of the metal precursors ($\text{Nb}(\text{C}_2\text{H}_5\text{O})_4$ and ZrOCl_2) in diluted aqueous ammonia solution. The samples were treated with 5–35 % hydrogen peroxide (Merck) in the pH range 2–4 at room temperature to generate ROS, and dried at room temperature in air prior EPR measurements. Nickel-exchanged ZSM-5 zeolite (Si/Al = 15, Zeolyst, Inc.) was obtained by ion exchange in aqueous $\text{Ni}(\text{NO}_3)_2$ solution, as explained elsewhere [29]. Chemical analysis by means of AAS method revealed the Ni/Al exchange degrees of 54 % (1.10 Ni wt%). Prior to adsorption of O_2 and CW-EPR measurements, the samples were activated in vacuum of 10^{-5} mbar at 773 K for 2 h, followed by reduction with CO (Aldrich, 99.95 %) at 673 K for 30 min [30]. Dealuminated zeolite SiBEA (Si/Al = 1000) was obtained from zeolite BEA (Si/Al = 11, RIPP China) by treating with 13 M HNO_3 solution (4 h, 353 K). The resulting sample was then contacted with a dilute aqueous solution of NH_4VO_3 (10^{-3} M, pH 2.4) at

room temperature [31]. In such conditions, the prevailing VO_2^+ cations react with the silanol groups of the dealuminated SiBEA. Chemical analysis of the sample revealed a vanadium loading of 0.9 wt%. As shown in our previous paper, vacuum treatment of such a sample at 773 K resulted in formation of paramagnetic VO_2 molecules that are clathrated in the zeolite channels [32].

EPR spectra were recorded at 77 K with an X-band Bruker ELEXSYS-580 spectrometer, using a rectangular TE_{102} cavity and 100 kHz field modulation. The spectra processing was performed with the software provided by Bruker, whereas for the computer simulations the EPRsim32 program was used [33]. It calculates exact solutions for the spin-Hamiltonian by full matrix diagonalization. A hybrid search procedure combining genetic algorithm and Powell refinement was applied for optimization of the simulated spectra.

In the case of mayenite, Nb_2O_5 , and ZrO_2 , prior to the measurements the samples were sealed in quartz tubes and outgassed in a vacuum line of $p < 10^{-3}$ mbar for 2 h at room temperature. Whereas for the zeolite samples, the superoxide radicals were generated by exposure of the thermally activated samples to 1–2 Torr of the naturally abundant (Aldrich, 99.95 %) or the ^{17}O -enriched dioxygen (Icon Service Inc., New Jersey, USA).

DFT calculations of \mathbf{g} tensors components and molecular diagrams of the magnetic-field induced couplings that show molecular orbital contributions to the g_{ii} elements ($g_{ii} = g_e + \Delta g_{ii}$) were performed for electrostatic, $q\text{-O}_2^-$ ($q = +1e, +2e, +3e, +4e$), and covalent $[\text{Ni-O}_2]^+$ adducts. For this purpose the one-component approach of Schreckenbach and Ziegler based on Pauli Hamiltonian [34] implemented in the ADF software [35] was utilized. The \mathbf{g} tensor values were also calculated within the mean-field approximation for the spin-orbit coupling (SOMF) implemented in the ORCA software [36]. More computational details can be found elsewhere [37].

3 Results and Discussion

3.1 EPR Spectroscopy of Surface Superoxide Species

The EPR spectra of the rigid superoxide species enriched in ^{17}O ($I = 5/2$) and trapped on the surface can be described in terms of the following spin-Hamiltonian:

$$\mathbf{H}_S = \hbar^{-1} \mu_B \mathbf{B}^T \cdot \mathbf{g} \cdot \mathbf{S} + \hbar^{-2} \mathbf{S} \cdot \mathbf{O} \mathbf{A} \cdot \mathbf{I}_O + \hbar^{-2} \mathbf{S} \cdot \mathbf{M} \mathbf{A} \cdot \mathbf{I}_M \quad (1)$$

where the \mathbf{g} tensor gauges the electronic Zeeman interaction, whereas the $\mathbf{O} \mathbf{A}$ tensor corresponds to the oxygen-17 hyperfine, and the $\mathbf{M} \mathbf{A}$ tensor to the possible metal

superhyperfine interactions between the corresponding nuclear spin \mathbf{I} and the electron spin \mathbf{S} . For the powder samples characteristic features in the EPR spectra appear when $\partial B / \partial \theta = 0$ and $\partial B / \partial \phi = 0$, where B is the resonant magnetic field $B(\theta, \phi) = \hbar \nu / g(\theta, \phi) \mu_B$ (when $I = 0$), ν is the microwave frequency, and θ and ϕ represent angles of polar coordinates showing orientation of principal \mathbf{g} tensor axes with respect to external magnetic field \mathbf{B} [38].

The three possible solutions, $\theta = 0$ (B_z), $\theta = \pi/2$ and $\phi = 0$ (B_x), $\theta = \pi/2$ and $\phi = \pi/2$ (B_y), correspond to the usual principal g_{zz} , g_{xx} and g_{yy} components of the \mathbf{g} tensor of the $^{16}\text{O}_2^-$ species, respectively (Fig. 1a). For each of these principal directions, the EPR signal is additionally split into $2I + 1 = 6$ lines in the case of the $^{16}\text{O}^{17}\text{O}^-$ isotopomer (Fig. 1b), and into $2nI + 1 = 11$ lines (with the intensity distribution 1:2:3:4:5:6:5:4:3:2:1) for the $^{17}\text{O}^{17}\text{O}^-$ isotopomer with equivalent nuclei (Fig. 1c). It is characteristic of the η^2 side-on binding of the superoxide moiety (Fig. 2a). For double labeled $^{17}\text{O}^{17}\text{O}^-$ species with nonequivalent oxygen atoms, the number of hyperfine features increase to $(2I + 1) \times (2I + 1) = 36$ lines of equal intensity (apart from the case of overlapping lines) at each direction (Fig. 1d). Such a splitting scheme is characteristic of the η^1 end-on superoxide adducts (Fig. 2b).

Because the nuclear magnetic moment of the ^{17}O nucleus is negative ($g_O = -0.75752$), the successive hyperfine lines appearing with the increasing magnetic field are transitions from $m_I = 5/2$ to $m_I = -5/2$, for singly-labeled species, and from $m_I = 5$ to $m_I = -5$ for doubly-labeled species, respectively, where m_I is the nuclear magnetic spin number. For the doubly labeled ($^{17}\text{O}-^{17}\text{O}$) $^-$ species, it is sensible to define a total nuclear spin number $I = I_1 + I_2 = 5$ as a convenient label for the hyperfine transitions. As a result, beside the sextet with equally intense lines due to the $^{16}\text{O}^{17}\text{O}$ molecules, there is a structure of 11 lines due to the $^{17}\text{O}^{17}\text{O}$ molecules (Fig. 1b, c). Because of the simultaneous appearance of all isotopomers, there are in principle 51 hyperfine lines in total to be expected for all \mathbf{g} tensor components, which often due to line crowding and overlapping may not all be resolved (Fig. 1e).

The intensity of these lines and their detectability can be controlled with the degree of the O-17 isotopic enrichment level p . The relative abundances (P^{nm}) of the $^{16}\text{O}_2$, $^{17}\text{O}^{16}\text{O}$, and $^{17}\text{O}_2$ isotopomers in the gas mixture are given by: $P^{16-16} = (1 - p)^2$, $P^{16-17} = 2p(1 - p)$, and $P^{17-17} = p^2$. At low enrichment levels (20–30 %), the signal due to the singly labeled molecules is dominant, while for mixtures with 60–70 % enrichment, the hyperfine patterns from both, singly and doubly labeled superoxide radicals, can be simultaneously observed giving rise to a complex EPR spectrum. It becomes dominated by the $^{17}\text{O}_2$ isotopomer for p above 80 %. Thus, for distinguishing between η^2

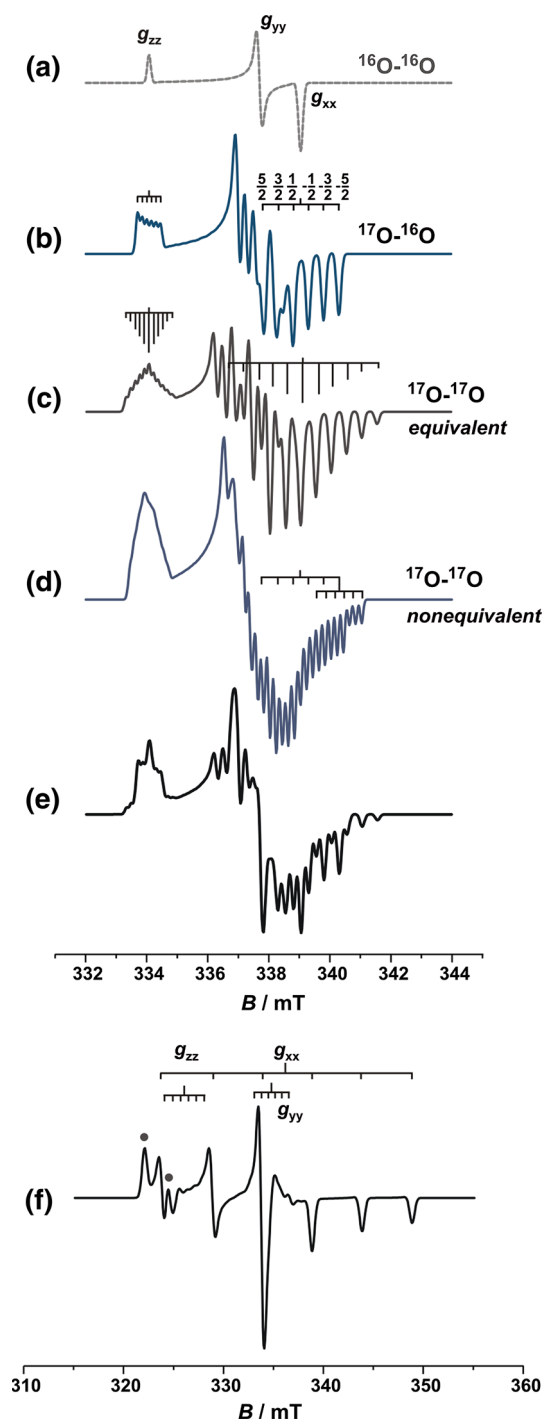


Fig. 1 Simulated CW-EPR powder spectra of superoxide species for: **a** $^{16}\text{O}_2$ isotopomer in rhombic environment **b** $^{16}\text{O}-^{17}\text{O}$ isotopomer, **c** $^{17}\text{O}-^{17}\text{O}$ isotopomer with equivalent nuclei, **d** $^{17}\text{O}-^{17}\text{O}$ isotopomer with nonequivalent nuclei, **e** weighted sum of $^{16}\text{O}-^{16}\text{O}$, $^{16}\text{O}-^{17}\text{O}$, and $^{17}\text{O}-^{17}\text{O}$ for enrichment level $p = 0.5$, and **f** $^{16}\text{O}-^{17}\text{O}$ for rhombic symmetry with extra features indicated with dots that appear upon an increase of the g tensor anisotropy

(side-on) and η^1 (end-on) coordination, higher O-17 enrichment levels with a dominant contribution from the double-labeled $^{17}\text{O}-^{17}\text{O}$ are required. The analysis of the

experimental spectrum should be carried out by adding the component signals of the three isotopomers ($^{16}\text{O}-^{16}\text{O}$) $^-$, ($^{17}\text{O}-^{16}\text{O}$) $^-$, and ($^{17}\text{O}-^{17}\text{O}$) $^-$ sharing the same g and A tensors, but weighted by their relative abundance P in the gas mixture (Fig. 1e).

This relatively simple situation becomes complicated in the powder samples when there is a large anisotropy of the g and ^{17}O A tensors. In conjunction with the high nuclear spin quantum number $I = 5/2$, this situation favors the appearance of the extra lines in the powder spectrum (Fig. 1f), when the following inequalities are satisfied [39]:

$$2A_i^2 - \hbar v A_i / m_I < (g_i^2 A_i^2 - g_j^2 A_j^2) / (g_i^2 - g_j^2) < 2A_j^2 - \hbar v A_j / m_I \quad (2)$$

These extra features correspond to additional solutions for $\partial B / \partial \theta = 0$ and $\partial B / \partial \phi = 0$ in the ij plane, and appearance of extra lines in the EPR spectrum that can exhibit quite significant intensity in comparison to the “normal” hyperfine pattern (vide infra).

Apart from the extra line effects, another conceivable complication of the powder EPR spectra of surface superoxide species stems from possible non-coincidence of the g and A tensors (low-symmetry features). This can be expected for superhyperfine coupling with magnetic metal centers M ($I \neq 0$) constituting the adsorption site, when the unpaired electron is mainly confined to the end-on η^1 superoxide ligand, or in the case of the hyperfine structure coming from $^{17}\text{O}_2^-$, when the unpaired electron is delocalized predominantly on the metal center M and, thus, defines the g tensor nature. For the analysis of such a metal superhyperfine coupling only those symmetry elements (Fig. 2a, b), which are shared between the corresponding magnetic nucleus and the magnetophore (the part of the superoxide adduct on which the spin density is delocalized, Fig. 2c) determining the g tensor, are decisive [40].

For axial (one C_n/D_n axis with $n \geq 3$, D_{2d}) or orthorhombic (C_{2v} , D_{2h}) symmetries both g and A tensors share the same principal axes, while in monoclinic (C_2 , C_s , C_{2h}) or triclinic (C_1 , C_i) symmetries the orientation of g and A axes may be different. However, for powder EPR spectra the relative orientations of the principal axes of the g and A tensors can only be determined for the monoclinic case, provided that $I > 1$ and both tensors exhibit large anisotropies. Then, taking as an example a hypothetical low-spin $\text{Co(III)}-\text{O}_2^-$ adduct with $I = 7/2$, for small $|m_I|$ values ($\pm 1/2$), the magnetic field extrema ($\partial B / \partial \theta = 0$ and $\partial B / \partial \phi = 0$), associated with the characteristic features in the powder spectra, occur at the angles close to the principal axes of the g tensor, whereas for large $|m_I|$ values ($\pm 7/2$), they appear at the angles close to the hyperfine principal axes. The result of such competition is the presence of hyperfine lines with strong variation in spacing with m_I

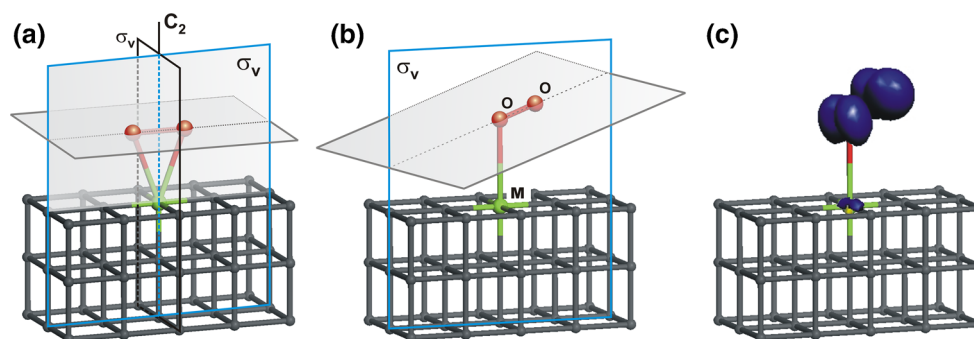


Fig. 2 Structural models of surface superoxide species of **a** C_{2v} (η^2) and **b** C_s (η^1) local symmetry trapped at the metal site M with $I \neq 0$. Whereas O–O moiety possessing two perpendicular planes exhibits a local C_{2v} point symmetry, only the vertical plane is shared with the M center, lowering the overall symmetry of the whole $M-O_2^-$

magnetophore to C_s . As a result it is expected that the g and ^{17}O hyperfine tensors are coincident, but the metal superhyperfine tensor MA is not. **c** Calculated spin density contour for surface $Ca^{2+}-O_2^-$ magnetophore

(Fig. 3). Another simple criterion of non-coincident axes is the presence of lines which are unaccounted for, lack of lines at positions anticipated from simple extrapolation starting from either side of the spectrum or failure to simulate spectra with correct line positions and intensities [41].

Even if in favorable situations it is possible to observe CW-EPR features smaller than 0.1 mT for the surface paramagnets [42], usually resolution is a crucial problem, particularly for the catalytic materials of high surface area. Often not all of the theoretically possible hyperfine lines may actually be resolved. By reading out the positions of characteristic spectral features, fairly accurate (within the first order) values of the EPR parameters can be extracted

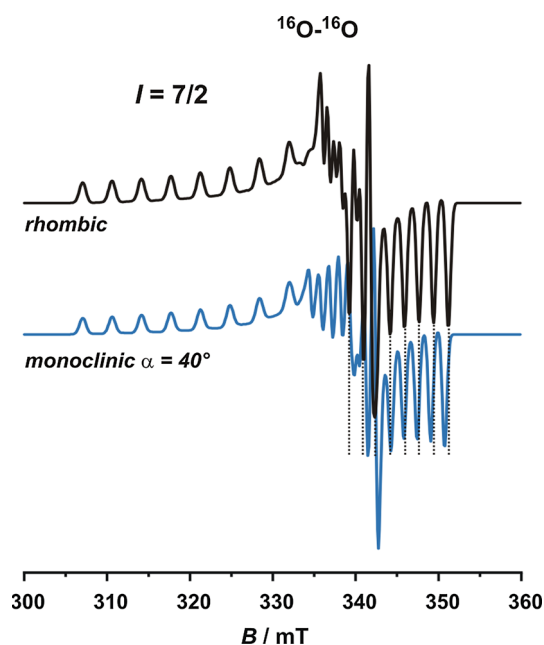


Fig. 3 Simulated CW-EPR powder spectra of hypothetical $^{16}O_2^-$ superoxide bound to a metal center of $I = 7/2$ nuclear spin. The symmetry assumed for simulation is rhombic or monoclinic with noncoincidence angle $\alpha = 40^\circ$ in xy plane

only in simple cases, when signals are not too complex, satisfactorily well resolved, and the axes are coincident [43]. For more complicated powder EPR spectra of surface superoxide species the line positions generally are not strictly linear in any of the magnetic parameters. Then computer simulation is the only way of reliable analysis of such spectra. For this purpose computer programs of various sophistication level, such as EPRsim32 [33] or EasySpin [44], are available.

3.2 Principal Mechanisms of O_2^- Formation and Varieties of Superoxide EPR Spectra

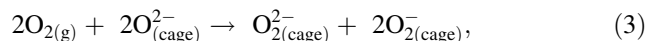
The shapes of the EPR spectra of the surface superoxide species depend on the chemical nature and the nuclear spin of the atoms that are in the intimate contact, as well as on the symmetry of the nearest surroundings [10]. As mentioned above, two generic forms include the η^1 end-on and the η^2 side-on geometries of the superoxide moieties that can be attached to the surface active center(s) via electrostatic or covalent bonds. When magnetic nuclei are present, the EPR spectrum is additionally featured by the hyperfine ($O-17$ labelled dioxygen) or the superhyperfine structure (metal centers with $I \neq 0$). Depending on the local symmetry of the resultant magnetophore the experimental EPR spectra may be categorized into axial, rhombic, mono-, and triclinic symmetry. In the latter two cases, the principal axes of the g and A tensors are not coincident, which may give rise to complicated features in the EPR spectrum that can properly be analyzed by computer simulation only. Axial symmetry of the EPR signal ($g_{zz} = g_{\parallel}$ and $g_{xx} = g_{yy} = g_{\perp}$) of the superoxide species is rather uncommon, and frequently results from unresolved g_{xx} and g_{yy} components due to line broadening or their dynamic averaging by rapidly tumbling O_2^- species on the surface [41].

Typical powder X-band EPR spectra of selected superoxide species trapped on various catalytic surfaces are

shown in Fig. 4. The collected examples include the O_2^- radicals (i) stabilized within the nano-cavities of highly ionic nature $[\text{Ca}_{24}\text{Al}_{28}\text{O}_{64}]^{4+}(\text{O}_2^{2-})$ (mayenite), (ii) exhibiting weak covalent interactions with the transition-metal ions (amorphous ZrO_2 and Nb_2O_5), (iii) species with significant covalent bonding interaction with the adsorption center (Ni(I)/ZSM-5), (iv) charge-transfer complexes VO_2/SiBEA , $\text{Mo(V)}/\text{SiO}_2$, $\text{Co(II)}/\text{MgO}$. They cover either the side-on (Ni(I)/ZSM-5, MgO , $[\text{Ca}_{24}\text{Al}_{28}\text{O}_{64}]^{4+}(\text{O}_2^{2-})$) and end-on structures ($\text{Co(II)}/\text{MgO}$, $\text{Mo(V)}/\text{SiO}_2$). Their spin-Hamiltonian parameters (g and hyperfine A tensors) are listed in Table 1.

The powder EPR spectrum of the mayenite sample (Fig. 4a) shows an orthorhombic signal characteristic of O_2^- trapped on the Ca^{2+} cations in the η^2 side-on fashion within the nanocavities [45, 46]. Its analysis via computer simulation allowed extraction of the g tensor components ($g_{zz} = 2.078$, $g_{yy} = 2.012$, and $g_{xx} = 2.005$), which are in a nice accordance with predictions of the Känzig–Cohen

model (vide infra). The O_2^- species are formed during the calcination as charge balancing anions (together with O_2^{2-} , O_2^- or OH^-) according to the *anionic redox processes* such as



and are encaged in the mayenite nanocavities, since its framework is positively charged, in contrast to the akin zeolites [45].

The superoxide radicals stabilized on amorphous ZrO_2 and Nb_2O_5 oxides (Fig. 4b, e, respectively) were generated by contacting the oxide samples with aqueous H_2O_2 solutions. The efficiency of O_2^- formation depends on pH of the reacting mixture, and the highest concentration of the O_2^- species was obtained for pH in the vicinity of the isoelectric point (IEP) of the oxide [21]. Based on the concerted in situ and spin trapping EPR measurements we proposed that O_2^- species are generated via *electroprotonic reaction*

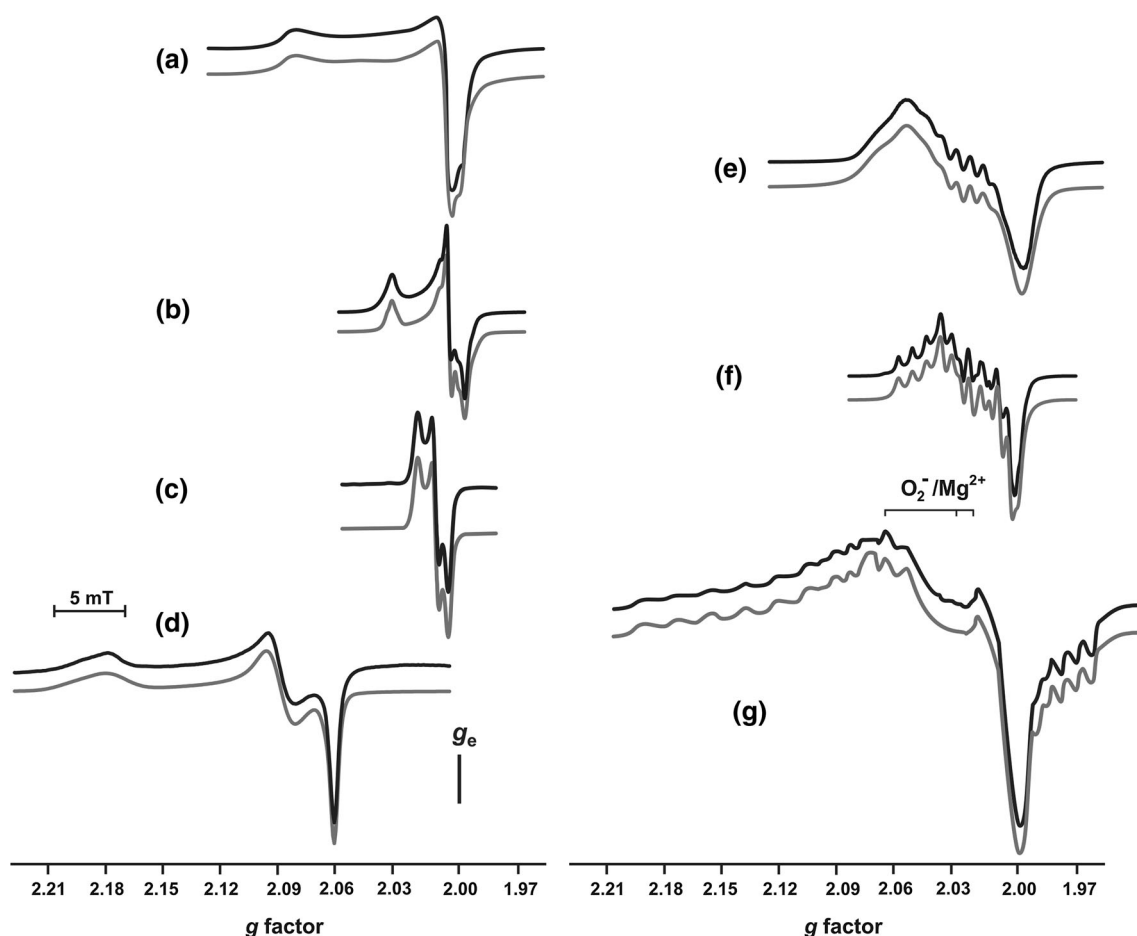


Fig. 4 EPR spectra (77 K) of superoxide species supported on catalytic materials. **a** Mayenite (calcium aluminate $12\text{CaO} \cdot 7\text{Al}_2\text{O}_3$), **b** amorphous ZrO_2 , **c** $\text{MoO}_x/\text{SiO}_2$, **d** Ni/ZSM-5 zeolite, **e** amorphous Nb_2O_5 , **f** VO_2/SiBEA zeolite, and **g** Co/MgO . Experimental

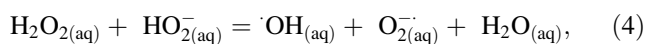
spectra—black lines, simulated spectra—gray lines. All spectra are presented with a common g -value scale. Spectra adapted from [27] (a), [49] (c), [30] (d), [21] (e), [53] (g)

Table 1 Spin-Hamiltonian parameters for superoxide species adsorbed on surfaces of selected catalytic materials

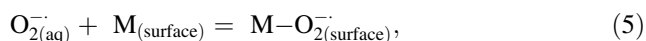
Sample	g_{xx}	g_{yy}	g_{zz}	$ A_{xx} $ (mT)	$ A_{yy} $ (mT)	$ A_{zz} $ (mT)	References
$[\text{Ca}_{24}\text{Al}_{28}\text{O}_{64}]^{4+}(\text{O}_2^{2-})$ (mayenite)	2.005	2.012	2.078				[27]
Mo/SiO ₂	2.005	2.011	2.018				[49]
Nb ₂ O ₅ ^a	2.0000	2.0208	2.0360	not resolved	1.00	not resolved	This paper
ZrO ₂	2.0025	2.0092	2.0317				This paper
Ni(I)/ZSM-5 ^b	2.0635	2.0884	2.1675	~1.0	5.67	~1.3	[30]
VO ₂ /SiBEA ^a	2.0054	2.0113	2.0239	0.53	0.68	0.98	this paper
MgO ^b	2.0016	2.0083	2.0770	7.63	0.72	0.83	[51]
Co/MgO ^a	2.000	2.033	2.141	1.5	0.7	3.1	[53]

^a Hyperfine parameters due to metal nuclear spin ($^{\text{Nb}}I = 9/2$, $^{\text{V}}I = 7/2$, $^{\text{Co}}I = 7/2$)

^b Hyperfine parameters due to oxygen-17 nuclear spin ($I = 5/2$)

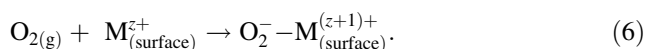


followed by trapping of superoxide species at the oxide surface



where M = Zr or Nb. The superoxide and hydroxyl radicals generated in the liquid phase were simultaneously detected by EPR with the aid of a DMPO spin trap. The EPR spectrum of O_2^- stabilized on ZrO_2 (Fig. 4b) exhibits a rhombic signal with the g tensor anisotropy (Table 1) characteristic of high oxidation state of the Zr^{4+} center inferred from the position of the g_{zz} component [18], as explained below in more detail. In the case of amorphous Nb_2O_5 (see Fig. 4e), an additional clearly resolved super-hyperfine structure due to ^{93}Nb ($I = 9/2$, 100 %) is observed only in one of the principal A tensor directions ($|A_{yy}| = 1$ mT, with A_{xx} and A_{zz} remaining unresolved), proving definitely that the superoxide species is attached directly to the Nb(V) center. The spin-Hamiltonian parameters of this adduct are intermediate between those expected for electrostatically [10, 45, 47] and covalently [26, 30] bound O_2^- species. Yet, they clearly indicate formation of the surface superoxide $\text{Zr(IV)}-\text{O}_2^-$ and $\text{Nb(V)}-\text{O}_2^-$ adducts. Analogous reactivity toward H_2O_2 was recently described for TiAlPO-5 molecular sieves showing formation of $\text{Ti}^{4+}-\text{O}_2^-$ species with $g_{zz} = 2.0212$, $g_{yy} = 2.0098$, and $g_{xx} = 2.0033$ [48].

Paramagnetic superoxide intermediates are often encountered when catalytic surface reactions are initiated by an interfacial electron transfer from the metal center M to the ligated dioxygen (MLET) [49]



Such *cationic redox mechanism* is often observed in the case of dioxygen contacted with transition-metal ions

dispersed on oxides or molecular sieves [8, 15, 30, 49]. Quite often MLET is followed by spillover of the resulting superoxide species onto the support, favored by configurational entropy increase, especially upon temperature enhancement. Examples are provided by the variable temperature interaction of dioxygen with the surface of $\text{MoO}_x/\text{SiO}_2$ (Fig. 4c), VO_2BEA (Fig. 4d), NiZSM-5 (Fig. 4e) or CoO-MgO (Fig. 4f) catalysts.

Isolated Mo(V) centers of various coordination environment grafted on amorphous SiO_2 surface are capable of reductive ET activation of dioxygen [49]. The EPR signal of the corresponding O_2^- species is shown in Fig. 4c. Stabilization of superoxide on molybdenum centers and formation of an end-on charge-transfer $\eta^1 \text{O}_2^- - \text{Mo(VI)}$ complex was definitely resolved by using ^{95}Mo ($I = 5/2$) and ^{17}O isotopic labeling [49].

Metallozeolites that accommodate 3d ions act as efficient cationic redox centers for O_2 activation, and their three-dimensional channel structure makes the cage metal centers easily accessible for gaseous dioxygen [29, 30, 50]. In particular, intrazeolite nickel(I) sites generated in situ via reduction of oxo-nickel species with CO ($\text{Ni}^{2+} - \text{O} - \text{Ni}^{2+} + \text{CO} = 2\text{Ni}^+ + \text{CO}_2$), exhibit high affinity toward dioxygen capture. Adsorption of 2 Torr of $^{16}\text{O}_2$ at 298 K on such samples leads to development of a well resolved orthorhombic EPR signal (Fig. 4d) with distinctly different g values ($g_{xx} = 2.0635$, $g_{yy} = 2.0884$, and $g_{zz} = 2.1675$) as compared with other O_2^- anionoradicals (Table 1). It can be assigned to a covalently bound superoxide species, produced following the MLET route $\text{O}_{2(\text{g})} + \text{Ni(I)/ZSM-5} \rightarrow \text{O}_2^- - \text{Ni(II)/ZSM-5}$ [9]. As it was deduced from the changes in the EPR signal intensity with time, the superoxide radical is quite stable at ambient conditions, even upon subsequent evacuation. The η^2 side-on attachment of the O_2^- moiety to the nickel center was inferred from the parallel $^{17}\text{O}_2$ adsorption experiments (see below). It is

worth noting here, that the O_2^- -Ni(II)/ZSM-5 adduct exhibits a reversed g tensor ($g_e < g_{yy}$, $g_{xx} < g_{zz}$) and $^0A_{yy} \gg ^0A_{xx}$, $^0A_{zz}$, which is distinctly different from previously observed values for its close bioinorganic analogues (g_{xx} , $g_{yy} > g_{zz}$, A_{ii} unresolved). They also deviate dramatically from those of the side-on O_2^- electrostatic complexes, typified by the classic O_2^-/MgO adduct with $g_e \approx g_{xx}$, $g_{yy} < g_{zz}$, and $A_{xx} \gg A_{yy}$, A_{zz} [51] (Table 1). This discrepancy results from the combined effects of the η^2 attachment and pronounced covalency of the nickel–oxygen bonding, giving rise to unusual redistribution of the spin density within the Ni(II)– O_2^- moiety [30].

Notable intrazeolite superoxide adducts (Fig. 4f) were also observed by contacting O_2 with an intrazeolite VO_2 molecule of unique high electron and oxygen donor properties, generated in situ during thermal reduction of VO_2^+ exchanged into dealuminated BEA zeolite [32]. The clear hyperfine structure (Table 1) proves direct bonding of the O_2^- moiety to the vanadium ($^V I = 7/2$) core, revealing formation of a charge transfer $\text{VO}_2^+-\text{O}_2^-$ complex, stabilized by silanol nests of the dealuminated BEA. Successful computer simulation of the corresponding EPR spectrum could only be accomplished by assuming a local monoclinic C_s symmetry, with the non-coincidence angle ($\alpha = 16^\circ$) between the g and $^V A$ axes in the yz plane.

Another example of the low symmetry spectra of the covalently bound superoxide is provided by the variable temperature interaction of dioxygen with the surface of CoO-MgO , which acts as a heterogeneous oxygen carrier binding dioxygen reversibly [52]. At low temperatures ($T < 100$ K) surface electron transfer leads to reversible formation of the end-on $\eta^1 \text{O}_2^-$ -Co(III) adduct ($g_{zz} = 2.141$, $g_{xx} = 1.983$, $g_{yy} = 2.033$, $A_{zz} = 3.1$ mT, $A_{xx} = 1.5$ mT, $A_{yy} = 0.7$ mT), see Fig. 4g. Yet, upon raising the temperature to 290 K, the superoxide spills over onto MgO matrix, forming a side-on electrostatic $\eta^2 \text{O}_2^-$ - Mg^{2+} complex with $g_{zz} = 2.077$, $g_{yy} = 2.008$, $g_{xx} = 2.002$ [53]. The latter species, when O-17 dioxygen enriched at various levels is used, exhibit complex EPR spectra (Fig. 5a) due to the presence of extra hyperfine lines. Their appearance may be better understood by plotting the angular dependence of the resonant field B versus θ angle for the $^{17}\text{O}-^{16}\text{O}$ and $^{17}\text{O}-^{17}\text{O}$ isotopomers (Fig. 5a, bottom) [51]. The obtained “road maps” indicate that apart from the usual field extrema along the principal directions along the principal axes (corresponding to $\theta = 0^\circ$ and 90°), in the zx plane there are additional local off-axes turning points ($\theta = 22.7^\circ$, 28.8° , 38.3° , 51.6° , 72.5°), which gives rise to five extra absorption lines (indicated with dots). They are even more intense than the regular ones (see Fig. 5b). More detailed analysis of the unusual EPR spectral features can be found in recent review [54].

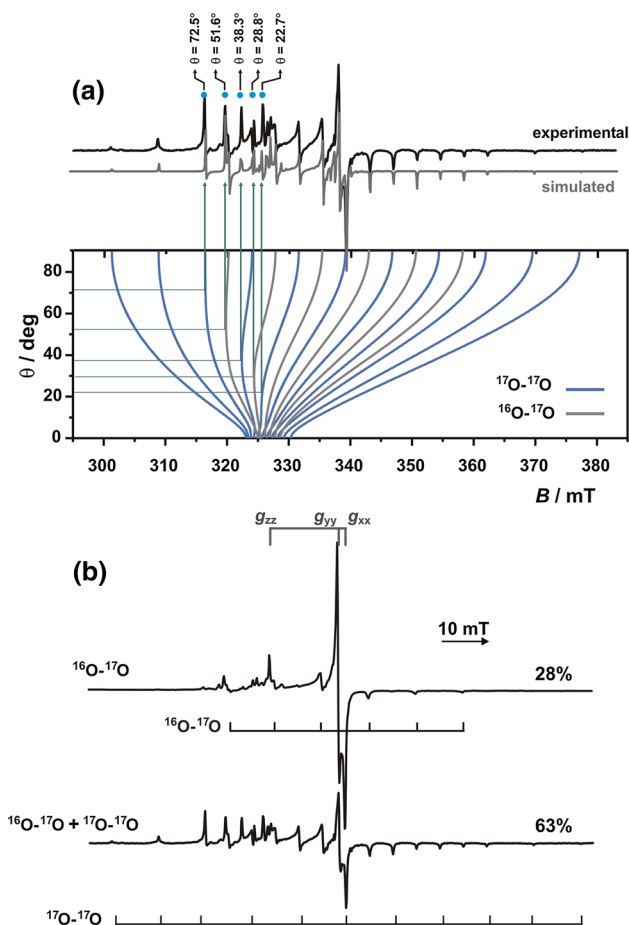


Fig. 5 **a** CW-EPR spectra of O-17 enriched superoxide radical stabilized on MgO surface and its relation with angular dependence of the resonant field B in the zx plane ($\phi = 0^\circ$), **b** dependence of the EPR spectra on the O-17 enrichment level (adapted from Ref. [51])

The overlapping extra and regular hyperfine lines make the superoxide EPR spectra complicated for analysis. Figure 5b illustrates clear advantage of using different isotopic enrichment to make the interpretation easier. The enrichment of $p = 28\%$ results in a dominant singly-labelled $^{16}\text{O}^{17}\text{O}$ species (6-line hyperfine pattern), while for $p = 63\%$ EPR signal due to the double-labelled $^{17}\text{O}^{17}\text{O}$ (11 lines) predominates. The number of the hyperfine lines appearing simultaneously can be then largely suppressed. However, despite these changes, the magnitude of their splitting (the 0A tensor) remains constant, helping in proper assignment of the hyperfine constants.

3.3 Electronic Nature of the Superoxide g Tensor: Electrostatic Adducts

The electronic nature of the experimental g tensor of the electrostatic superoxo complexes may be analyzed using the classic Känzig and Cohen model [55], at least as a first approximation. For the unbound O_2^- ($\sigma_g^2 \pi_u^4 \pi_g^{*3}$) radical, the

unpaired electron occupies two degenerate antibonding $\pi_g^*(2p)$ orbitals giving rise to the ${}^2\Pi_{3/2}$ ground state. In such a case the g tensor is extremely anisotropic with $g_{||} = 2\langle +1, +1/2 | L_z + 2S_z | +1, +1/2 \rangle = 4$ and $g_{\perp} = \langle +1, -1/2 | L_x + 2S_x | -1, +1/2 \rangle = 0$. As a result, the corresponding EPR signal of the randomly oriented free superoxide radicals will extend over a wide magnetic field, being too weak to be detected, unless the orbital momentum is partially quenched due to the interaction with the nearest chemical environment. The resultant bonding interaction localizes the odd electron on one of the $\pi_{(x,y)}^*g$ orbitals, while the crystal field distortion Δ gives rise to two states with the energies equal to $\pm \frac{1}{2}\lambda_O[1 + (\Delta/\lambda_O)^2]^{1/2}$, where λ_O is a free oxygen spin–orbit coupling.

This simple case can be exemplified by the O_2^- species stabilized on ionic surfaces such as MgO, where the local C_{2v} crystal field gives rise to an orthorhombic g tensor with $g_{zz} \gg g_{yy} > g_{xx} \approx g_e$, which is described by the following equations

$$\begin{aligned} g_{xx} &= g_e \cos 2\alpha - (\lambda/E)(1 - \sin 2\alpha - \cos 2\alpha), \\ g_{yy} &= g_e \cos 2\alpha - (\lambda/E)(\sin 2\alpha - \cos 2\alpha - 1), \\ g_{zz} &= g_e + 2l \sin 2\alpha, \end{aligned} \quad (7)$$

where $\tan 2\alpha = \lambda/\Delta$, $l = i\langle \pi_y^* | L_z | \pi_x^* \rangle$, $g_e = 2.0023$, and λ is the spin–orbit coupling constant, Δ is the splitting of both $\pi_g^*(2p_x)$ and $\pi_g^*(2p_y)$ levels, while E is the separation between the $\pi_g^*(2p_x)$ and $\sigma_g^*(2p_z)$ orbitals.

From the experimental g tensor values the molecular λ , Δ , and E parameters can then be derived. For instance, using the data from Table 1 for EPR spectrum of O_2^- encaged in the mayenite (Fig. 4a), the values of $\Delta = 0.44$ eV and $E = 3.04$ eV were calculated, which are typical for the superoxide radicals adsorbed on divalent cation centers [56]. This indicates that superoxide species are trapped on the Ca^{2+} and not on the Al^{3+} sites. The value of $\lambda = 0.0168$ eV, very close to the pure atomic one ($\lambda_O = 0.0167$ eV) implies that the O_2^- radical is essentially stabilized via through-space electrostatic interactions.

Much more detailed insight into the molecular nature of the g tensor can be obtained from relativistic theoretical calculations based on the ZORA, SOMF or Pauli Hamiltonian, reviewed by us recently [37]. ZORA–SOMF hybrid method reproduces the g and A tensor parameters with higher accuracy, however calculations based on the scalar Pauli Hamiltonian are particularly useful for their chemical interpretation. In this approach the calculated g_{ii} components may be partitioned in the following way: $\Delta g_{ij} = \Delta g_{ij}^{rel} + \Delta g_{ij}^d + \Delta g_{ij}^p$, where Δg_{ij}^{rel} combines scalar relativistic corrections, whereas the terms Δg_{ij}^d and Δg_{ij}^p stand for dia- and paramagnetic contributions to Δg_{ij} , respectively. The paramagnetic term (Δg_{ij}^p) dominates the g tensor values [57, 58], therefore, while analyzing the

molecular nature of their anisotropy it is enough to restrict the discussion to this overwhelming term only. The main contributions to Δg_{ij}^p are defined, in turn, by the magnetic field-induced couplings between the occupied and virtual magnetic orbitals ($\Delta g_{ij}^{p,occ-virt}$), accounting for more than 90 % of the total Δg shift. This may be deduced from the non-vanishing elements of the following integrals [57]:

$$\Delta g_{ij}^{p,m-n} \propto \frac{1}{2c(\varepsilon_n^\sigma - \varepsilon_m^\sigma)} \langle \Psi_m^\sigma | iL_{i=x,y,z} | \Psi_n^\sigma \rangle \quad (8)$$

where Ψ_m and Ψ_n are the unperturbed Kohn–Sham orbitals, ε are the magnetic MO energies, $L_{i=x,y,z}$ is the orbital momentum operator, whereas σ stands for α or β spin. To simplify construction of the MO coupling diagrams that are used to interpret the g tensor anisotropy (Figs. 6, 7), only the most important contributions (exceeding 10 % of the total Δg_{ij}) were taken into account.

The purely electrostatic interaction of the superoxide species with the adsorption sites can be modeled with the simplest discrete $\eta^2\text{-}\{O_2^--q\}$ and $\eta^1\text{-}\{O_2^--q\}$ side-on and end-on reference adducts, respectively, for $q = +1, +2$, etc. In such a case the DFT calculations can be compared directly with the popular Känzig and Cohen semi-empirical treatment of the g tensor of the bound O_2^- (${}^2\Pi_{3/2}$) species (vide supra).

As shown by the spin-restricted Pauli calculations, even for the simplest electrostatic $\eta^2\text{-}\{O_2^--q^{2+}\}$ epitome of the C_{2v} point symmetry (Fig. 6a), the obtained results ($g_{xx} = 2.002$, $g_{yy} = 2.012$, $g_{zz} = 2.079$) are in a surprisingly good agreement with the experimental data observed for the real $\eta^2\text{-}\{O_2^--Ca^{2+}\}$ /mayenite or $\eta^2\text{-}\{O_2^--Mg^{2+}\}$ /MgO highly ionic systems (Table 1). The g_{xx} value remains intact ($g_{xx} \cong g_e$), since in the C_{2v} point group the spin–orbit coupling of the SOMO with the $9b_1(\pi_x^*)$ and $6a_1(\sigma_{2p})$ states is forbidden for L_x operator by symmetry. The g_{yy} component is featured by one relatively small coupling between the occupied $6a_1(\sigma_{2p})$ and the semi-occupied $9b_1(\pi_x^*)$ orbitals only, and it may be identified with the E parameter in the Känzig–Cohen approach. The shift of the most sensitive g_{zz} component arises from the strong coupling between the $8b_2(\pi_y^*)$ and $9b_1(\pi_x^*)$ orbitals, which corresponds to the Δ parameter. The coupling scheme in Fig. 6a accounts well for the $g_{zz} \gg g_{yy} > g_{xx} \approx g_e$ sequence (predicted adequately already by the Känzig and Cohen treatment), and experimentally observed for most of the electrostatically bound superoxo species on ionic surfaces, where the simple crystal field account is valid [9].

A similar coupling scheme is observed for the end-on $\eta^1\text{-}\{O_2^--q^{2+}\}$ epitome of C_s point symmetry (Fig. 6b). A distinct difference between the η^2 and η^1 binding schemes is a larger splitting between the involved magnetic orbitals for η^1 , resulting in smaller anisotropy of the g tensor (in accordance with Eq. 8). This phenomenon affects mostly

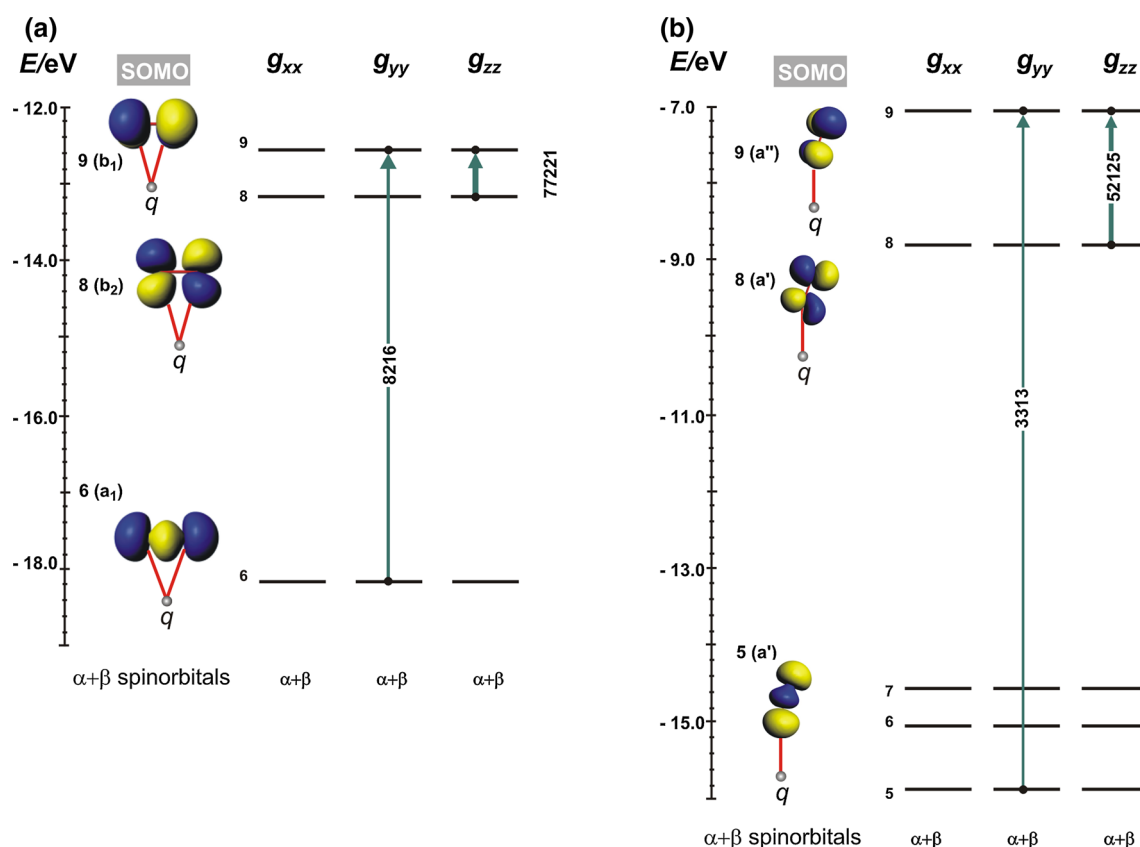


Fig. 6 Magnetic field-induced molecular orbital diagram for the most important paramagnetic contributions to the g tensor components of **a** η^2 - $\{\text{O}_2^- - q\}$ and **b** η^1 - $\{\text{O}_2^- - q\}$ electrostatic adducts ($q = +2e$), in

spin-restricted scalar relativistic Pauli Hamiltonian calculations. The molecular orbital couplings are indicated with arrows, and the corresponding contributions are given in ppm

the g_{zz} component ($g_{zz} = 2.077$ for η^2 and 2.053 for η^1 binding mode), decreasing also the $g_{xx} - g_{yy}$ anisotropy. As a result, the EPR spectra of the end-on adducts show a tendency toward more apparent axial shape.

3.4 Electronic Nature of the Superoxide g Tensor: Covalent Adducts

A more involved situation with respect to the ionic environments can be anticipated for the more covalent O_2^- -Ni(II)/ZSM-5 adduct, as it may be deduced already from its pronounced g tensor anisotropy (cf. the EPR spectra in Fig. 4). In comparison to the electrostatically attached O_2^- , all the g tensor components of this adduct are substantially shifted toward higher g values. This is a consequence of direct involvement of the nickel-based states into the magnetic couplings, but for the most part, also due to the appearance of new magnetic transitions. They are shown in the molecular diagram for the discrete η^2 - $\{\text{O}_2^- - \text{Ni(II)}\}$ unit (Fig. 7). The g_{xx} component (equal to g_e in the electrostatic model) is now affected by two couplings $17b_2$ - $(d_{xz} + \pi^*) \leftrightarrow 22a_2(d_{x^2-y^2} - \pi^*)$ and $22a_2(d_{x^2-y^2} - \pi^*) \leftrightarrow$

$23b(d_{xz} - \pi^*)$, whereas the Δg_{yy} shift is dominated by the $20b_1(d_{yz} - \pi^*) \leftrightarrow 22a_2(d_{x^2-y^2} - \pi^*)$ transition. The contributions to the g_{zz} value include two strong $21a_1$ - $(d_{z^2} - \pi^*) \leftrightarrow 22a_2(d_{x^2-y^2} - \pi^*)$ and $18a_1(d_{z^2} - \sigma) \leftrightarrow 22a_2(d_{x^2-y^2} - \pi^*)$ magnetic transitions. As a result, all the g_{ii} components acquire a pronounced mixed metal–ligand nature involving mostly the coupling of the SOMO with the relevant occupied states. This picture explains quantitatively large positive shifts of all g tensor components for the η^2 - $\{\text{Ni(II)}-\text{O}_2^-\}$ adduct (actually observed experimentally), and their distinctly different molecular character featured by $g_{zz} > g_{xx} > g_{yy} > g_e$, in comparison to the electrostatic η^2 - $\{q^{2+}-\text{O}_2^-\}$ analogue. The observed peculiarities arise mainly from the δ -type overlap of the out of plane π^*_\perp orbital of dioxygen moiety with the $d(x^2 - y^2)$ orbital of the nickel center, allowed in the η^2 geometry.

Apart from the bonding geometry, also the charge of the adsorption site strongly influences the EPR g tensor anisotropy of the bound O_2^- . The calculated (SOMF-B3LYP) g_{ii} elements for η^1 - $\{\text{O}_2^- - q\}$ with the increasing charge q (Fig. 8a) show a systematic decrease of g_{zz} value up to $q = +3e$. Such an effect was also observed experimentally

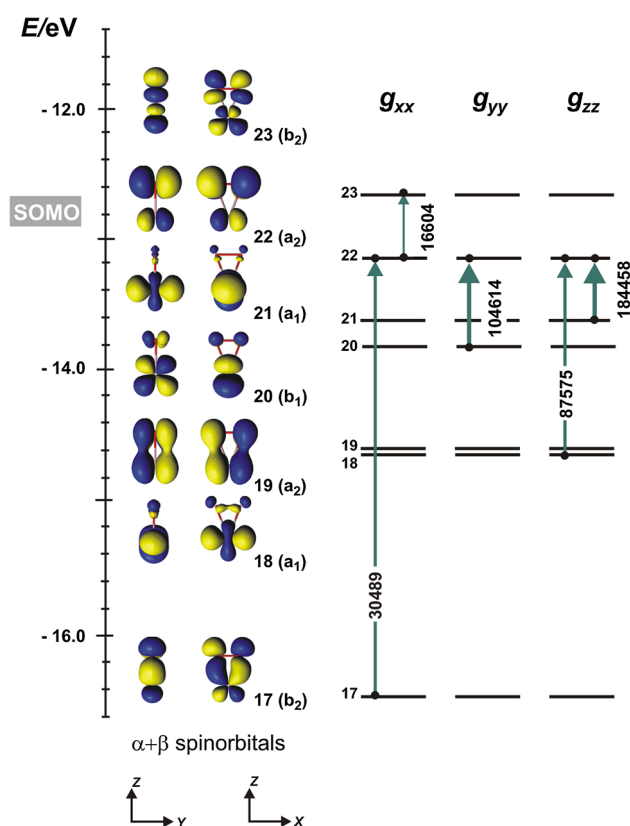


Fig. 7 Magnetic field-induced molecular orbital diagram for the most important paramagnetic contributions to the g tensor components of $\eta^2\text{-}\{\text{O}_2^-\text{-Ni(II)}\}$ magnetophore, within the spin-restricted scalar relativistic Pauli Hamiltonian calculations. The couplings are indicated with arrows and the corresponding contributions are given in ppm

for a series of superoxide adducts with Na^+ , Mg^{2+} , and Sc^{3+} cations in a frozen MeCN solution [59]. The SOMF (Fig. 8a) and Pauli (Fig. 6b) calculations shows that the most sensitive g_{zz} value decreases systematically with charge from 2.115 ($q = +1e$) to 2.077 ($q = +2e$) and 2.023 ($q = +3e$). It is nicely accompanied by experimental values of 2.1106 (NaO_2 trapped in rare-gas matrix) [60], 2.24 (NaO_2/MgO) [61], and 2.1197 (CsO_2/MgO) [62] for the $q = +1e$ case; 2.0451, 2.0499, 2.0558, and 2.0587 ($\text{Mg}^{2+}\text{O}_2^-$, $\text{Ca}^{2+}\text{O}_2^-$, $\text{Sr}^{2+}\text{O}_2^-$, and $\text{Ba}^{2+}\text{O}_2^-$, respectively, in MeCN) [59] for the $q = +2e$ case; and 2.0304 ($\text{Sc}^{3+}\text{O}_2^-$ in MeCN) [59]. Although for the highest charge, $q = +4e$, a reversed g tensor is predicted ($g_{zz}, g_{yy} > g_{xx}$), such situation is chemically unlikely. Indeed, for VO_2 or MoO_x species, where the metals are formally tetra- and pentavalent, the experimental g_{ii} parameters (Table 1) resemble those of $q = +3e$, implying that the effective charge is actually lower due to strong covalency of the vanadyl/molybdenyl bonds, in accordance with the chemical intuition. With an increase of the charge, the orientation selectivity for the g_{zz} component (the value of the

resonant field $B(\theta, \phi)$) is partially lost, while in the xy plane almost all orientations of the paramagnets participate in resonance simultaneously.

The effect of charge of the adsorption site can be used, e.g., to follow spillover of the O_2^- species in the case of supported systems (such as $\text{Mo}^{(\text{VI})}\text{O}_x/\text{SiO}_2$) or dilute solid solutions (CoO-MgO). Time evolution of the superoxide species in $\text{Mo}^{(\text{VI})}\text{O}_x/\text{SiO}_2$ at 294 K (Fig. 8b) shows that O_2^- initially bound to Mo sites diffuses onto the SiO_2 support, which is indicated by the appearance of a new g_{zz} component at lower magnetic field. After 55 min at room temperature all the generated superoxide species are stabilized on the silica matrix.

In the case of polycrystalline samples, site sensitivity of the superoxide radical reflects the heterogeneity of the stabilization centers. This is probably best illustrated with O_2^- stabilized on powder MgO sample. The appearance of several lines in the g_{zz} region can be explained by the presence of the topologically distinct adsorption sites, localized on planes (O_{5c}), corners (O_{3c}) or edges (O_{4c}) of the MgO nanocrystals (Fig. 8c). Such sites exhibit slightly different effective charges, therefore also different values of the Δ splitting, which is nicely reflected in the multiplication of the g_{zz} component.

3.5 Analysis of Superoxide ^{17}O Hyperfine Tensor

As already discussed distinction between the η^1 and η^2 binding mode of the superoxide species can be at best resolved using the isotopically enriched dioxygen. Two examples that are invoked to illustrate this point include $\eta^2\text{-}\{^{17}\text{O}_2^-\text{-Ni(II)}\}$ adduct in ZSM-5 zeolite [30] and $\eta^1\text{-}\{^{17}\text{O}_2^-\text{-Mo(VI)}\}$ adduct supported on SiO_2 [49] (Fig. 9). The EPR spectrum and its simulation of the ^{17}O -enriched superoxo complex formed by reaction with Ni(I)/ZSM-5 centers is shown in Fig. 9a. The dioxygen bonding type is proved by the presence of the characteristic 11-line pattern in the g_{yy} direction, discernible better after magnification of the low- and high-field wings of the spectrum. Simulation of the $^{17}\text{O}\text{-}^{17}\text{O}$ component with two equivalent nuclei is shown in Fig. 9b. Although only the diagnostic A_{yy} splitting is well resolved, the values of the remaining A_{xx} and A_{zz} splittings are assessed with acceptable accuracy by computer simulation. These results confirm the $\eta^2\text{-}\{\text{O}_2^-\text{-Ni(II)}\}$ structure of the observed paramagnetic adduct.

From the unstructured rhombic EPR signal of the O_2^- species observed after adsorption of dioxygen on the $\text{MoO}_x/\text{SiO}_2$ surface (Fig. 9c), the oxygen binding mode cannot be safely deduced. Yet, the analysis of the hyperfine structure of the isotopically enriched oxygen (Fig. 9d) revealed the presence of two $^{16}\text{O}\text{-}^{17}\text{O}$ and $^{17}\text{O}\text{-}^{16}\text{O}$ isotopomers due to the linkage isomerism ($^{16}\text{O}^{17}\text{O}^-\text{-Mo}$ and $^{17}\text{O}^{16}\text{O}^-\text{-Mo}$) implying an end-on η^1 geometry [9]. It was

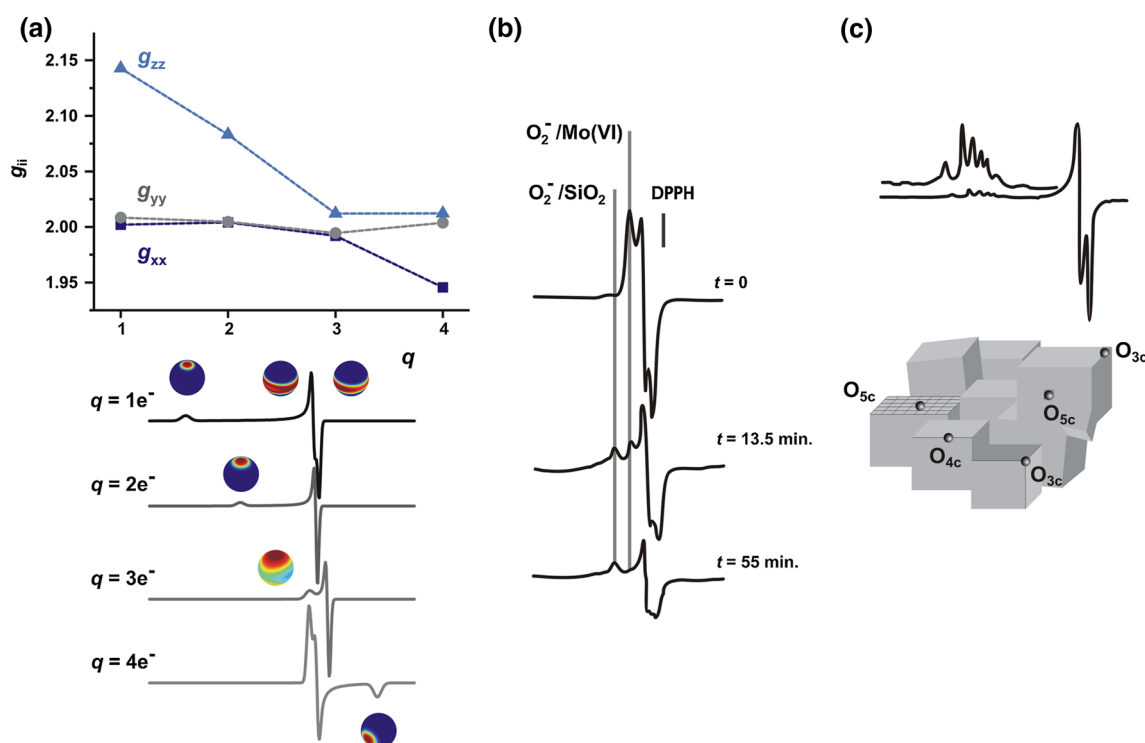
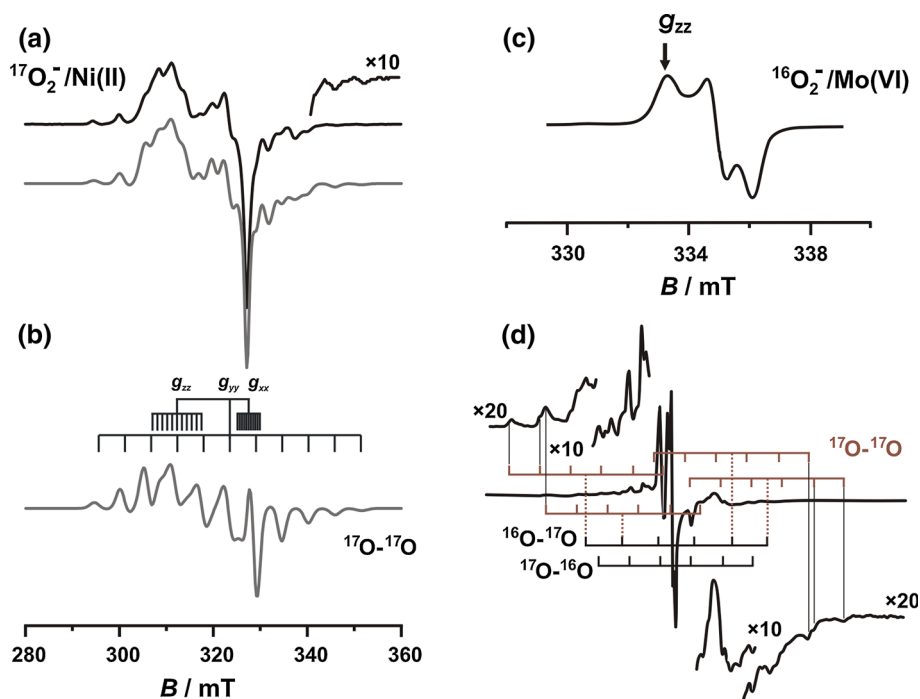


Fig. 8 **a** Dependence of the g tensor components of $\eta^1\text{-}\{O_2^--q\}$ species on the point charge value for $q = +1e^-$, $+2e^-$, $+3e^-$, and $+4e^-$, calculated with B3LYP-SOMF method along with the corresponding simulated powder EPR spectra. The unit spheres show orientation selectivity of particular magnetic field positions. **b** Sequence of EPR spectra (77 K) that illustrates spillover of O_2^- radicals from the

activation Mo centers toward silica matrix. **c** EPR spectrum of $^{16}O_2^-$ radicals on MgO showing how topographic speciation of superoxide species among adsorption sites of various coordination (O_{3c} , O_{4c} , O_{5c}) is revealed by the multiple g_{zz} component. Experimental spectra adapted from [49] (b) and [63] (c)

Fig. 9 EPR spectra (77 K) of **a** O-17 enriched superoxide adducts obtained after adsorption of $^{17}O_2$ (1 Torr) on Ni(I)/ZSM-5 zeolite. **b** Simulated $^{17}O\text{-}^{17}O$ component of EPR signal of isotopically enriched superoxide adduct. **c** O-16 and **d** O-17 enriched superoxide adducts with Mo(VI)/SiO₂ surface centers. Experimental spectra—black lines, simulated spectra—gray lines. Spectra adapted from [30] (a) and [49] (c, d)



further confirmed by the ^{17}O – ^{17}O isotopomer with two nonequivalent nuclei that give rise to the complex hyperfine structure comprising of 36 lines.

Once the $^{\text{O}}\text{A}$ tensor components are determined, redistribution of the spin density within superoxo moiety can be obtained by means of standard treatment using the simple formula $\rho^i = B_i/B_0$. In this equation $B_0 = -336.8$ MHz is the tabulated atomic value for the dipolar ^{17}O hyperfine constant [64], whereas B_i should be determined from the dipolar part of $^{\text{O}}\text{A}$ hyperfine tensor. Thus, such analysis requires decomposition of the experimental $^{\text{O}}\text{A}$ tensor into the isotropic (a_{iso}) and dipolar (T) terms,

$$^{\text{O}}\text{A} = a_{\text{iso}} + \text{T} = a_{\text{iso}} + \text{B}_y + \text{B}_x, \quad (9)$$

where the second and the third matrix is related to the dipolar contributions along y (B_y) and x (B_x) axis, respectively.

Using the $^{\text{O}}\text{A}$ tensor values obtained by spectra simulation for the $\eta^2\text{-}\{\text{O}_2\text{-Ni(II)}\}$ adduct (Table 1), such decomposition leads to: $^{\text{O}}\text{A}/\text{MHz} = [+28.88; -165.70; +39.44] = -32.46 + [+68.38; -136.80; +68.38] + [-7.04; +3.52; +3.52]$. The obtained value of $a_{\text{iso}} = -32.46$ MHz is in line with its dominant spin polarization origin, found earlier for the ionic O_2^- radicals trapped on MgO surfaces ($a_{\text{iso}} = -60.7$ MHz) [51]. In comparison to the ionic adducts, reduction of its magnitude, may be associated with a sizable shift of the spin density from the superoxo moiety to the nickel core (Fig. 7). The obtained $B_x = -7.04$ MHz and $B_y = -136.8$ MHz values corresponds to $\rho_x^{\pi} = 0.02$ and $\rho_y^{\pi} = 0.40$ spin densities. As a result, the dioxygen moiety in the $\eta^2\text{-}\{\text{O}_2\text{-Ni(II)}\}$ adduct bears 0.84 of the total spin density, confirming definitely its essentially superoxide nature. The remaining part of the spin density is redistributed on the nickel orbitals, giving rise to fairly even distribution of the spin density $\text{O}(0.42)\text{-O}(0.42)\text{-Ni}(0.16)$ within the magnetophore unit. It confirms also substantial covalency of the nickel–dioxygen bond reflected in the unusual g tensor parameters of the $\eta^2\text{-}\{\text{Ni(II)-O}_2\text{-}\}$ adduct, as compared with other superoxide complexes discussed in this paper. Analogous calculations for O_2^- stabilized on MgO ($\eta^2\text{-O}_2^-/\text{MgO}$) adduct with hyperfine tensor $^{\text{O}}\text{A}/\text{MHz} = [-213.93; +20.19; +23.98]$ gives $a_{\text{iso}} = -60.7$ MHz and $\text{T}/\text{MHz} = [-153.23; +80.89; +84.68]$ [51]. The resultant spin density on superoxide moiety equals 0.99 in accordance with nearly pure electrostatic nature of the surface adduct.

4 Conclusions

EPR spectroscopy combined with isotopic labelling is a powerful and very sensitive technique, which can be applied successfully to analysis of the superoxide intermediates in catalysis. It may resolve many problems related

with definite identification of O_2^- species, establishment of the end-on versus side-on attachment mode, and provide an insight into the intimate nature of the dioxygen-surface site bond via molecular interpretation of g and O-17 hyperfine tensors. Interpretation of EPR spectra based on the diagnostic features of the bound superoxide species was described. The typical semi-empirical method and DFT-based analysis of the corresponding parameters were also discussed. The formation of O_2^- species on heterogeneous surfaces was categorized into cationic and anionic redox mechanisms as well as electroprotic processes in the case of H_2O_2 as a reactant. The experimentally observed variety of superoxide EPR signals and the molecular nature of their parameters were accounted for by the electrostatic (magnitude of the charge, O_2 binding mode) and covalent effects.

Acknowledgments This research was financially supported by the Ministry of Science and Higher Education (MNiSW) of Poland, Grant No. Iuventus Plus IP2011 041871. The equipment used in this study was purchased thanks to the financial support of the European Regional Development Fund in the framework of the Polish Innovation Economy Operational Program (Contract No. POIG.02.01.00-12-023/08).

Open Access This article is distributed under the terms of the Creative Commons Attribution 4.0 International License (<http://creativecommons.org/licenses/by/4.0/>), which permits unrestricted use, distribution, and reproduction in any medium, provided you give appropriate credit to the original author(s) and the source, provide a link to the Creative Commons license, and indicate if changes were made.

References

1. Bielański A, Haber J (1991) Oxygen in catalysis. Marcel Dekker, New York
2. Prabhakar R, Siegbahn PEM, Minaev BF, Agren H (2002) Activation of triplet dioxygen by glucose oxidase: spin-orbit coupling in the superoxide ion. *J Phys Chem B* 106:3742–3750
3. Sojka Z (1995) Molecular aspects of catalytic reactivity. Application of EPR spectroscopy to studies of the mechanism of heterogeneous catalytic reactions. *Catal Rev Sci Eng* 37:461–512
4. Katakis D, Gordon G (1987) Mechanism of inorganic reactions. Wiley, New York
5. Harvey JN (2007) Understanding the kinetics of spin-forbidden chemical reactions. *Phys Chem Chem Phys* 9:331–343
6. Howe RF (1982) EPR spectroscopy in surface chemistry: recent developments. *Adv Colloid Interf Sci* 18:1–55
7. Che M, Giamello E (1990) Electron paramagnetic resonance. *Stud Surf Sci Catal* 57B:265–332
8. Dyrek K, Che M (1997) EPR as a tool to investigate the transition metal chemistry on oxide surfaces. *Chem Rev* 97:305–331
9. Che M, Tench AJ (1982) Characterization and reactivity of mononuclear oxygen species on oxide surfaces. *Adv Catal* 31:77–133
10. Che M, Tench AJ (1983) Characterization and reactivity of molecular oxygen species on oxide surfaces. *Adv Catal* 32:1–148
11. Chiesa M, Giamello E, Che M (2010) EPR characterization and reactivity of surface-localized inorganic radicals and radical ions. *Chem Rev* 110:1320–1347

12. Sheng Y, Abreu IA, Cabelli DE, Maroney MJ, Miller A-F, Teixeira M, Selverstone Valentine J (2014) Superoxide dismutases and superoxide reductases. *Chem Rev* 114:3854–3918
13. Bonini MG, Malik AB (2014) Regulating the regulator of ROS production. *Cell Res* 24:908–909
14. Avdeev VI, Bedillo AF (2013) Electronic structure of oxygen radicals on the surface of VO_x/TiO_2 catalysts and their role in oxygen isotopic exchange. *J Phys Chem C* 28:14701–14709
15. Smeets PJ, Woertink JS, Sels BF, Solomon EI, Schoonheydt RA (2010) Transition-metal ions in zeolites: coordination and activation of oxygen. *Inorg Chem* 49:3573–3583
16. Fujita S, Suzuki K, Ohkawa M, Mori T, Iida Y, Miwa Y, Masuda H, Shimada S (2003) Oxidative destruction of hydrocarbons on a new zeolite-like crystal of $\text{Ca}_{12}\text{Al}_{10}\text{Si}_4\text{O}_{35}$ including O_2^- and O_2^{2-} radicals. *Chem Mater* 15:255–263
17. Volodin AM, Zhidomirov GM, Dubkov KA, Hensen EJM, van Santen RA (2005) Spin design of iron complexes on Fe-ZSM-5 zeolites. *Catal Today* 110:247–254
18. Giamello E, Rumori P, Geobaldo F, Fubini B, Paganini MC (1996) The interaction between hydrogen peroxide and metal oxides: EPR investigations. *Appl Magn Reson* 10:173–192
19. Antcliff KL, Murphy DM, Griffiths E, Giamello E (2003) The interaction of H_2O_2 with exchanged titanium oxide systems (TS-1, TiO_2 , [Ti]-APO-5, Ti-ZSM-5). *Phys Chem Chem Phys* 5:4306–4316
20. Neumann R, Levin-Elad M (1997) Metal oxide (TiO_2 , MoO_3 , WO_3) substituted silicate xerogels as catalysts for the oxidation of hydrocarbons with hydrogen peroxide. *J Catal* 166:206–217
21. Ziolek M, Sobczak I, Decyk P, Sobańska K, Pietrzyk P, Sojka Z (2015) Search for reactive intermediates in catalytic oxidation with hydrogen peroxide over niobium(V) and tantalum(V). *Appl Catal B* 164:288–296
22. Anpo M, Che M, Fubini B, Garrone E, Giamello E, Paganini MC (1999) Generation of superoxide ions at oxide surfaces. *Top Catal* 8:189–198
23. Macyk W, Szacilowski K, Stochel G, Buchalska M, Kunciewicz J, Labuz P (2010) Titanium(IV) complexes as direct TiO_2 photosensitizers. *Coord Chem Rev* 254:2687–2701
24. Blezer L, Dröse S (2013) Superoxide generation by complex III: from mechanistic rationales to functional consequences. *BBA Bioenerg* 1827:1320–1331
25. Walling C (1975) Fenton's reagent revisited. *Acc Chem Res* 8:125–131
26. Cho J, Sarangi R, Nam W (2012) Mononuclear metal- O_2 complexes bearing macrocyclic *N*-tetramethylated cyclam ligands. *Acc Chem Res* 45:1321–1330
27. Maurelli S, Ruzsak M, Witkowski S, Pietrzyk P, Chiesa M, Sojka Z (2010) Spectroscopic CW-EPR and HYSCORE investigations of Cu^{2+} and O_2^- species in copper doped nanoporous calcium aluminate ($12\text{CaO} \cdot 7\text{Al}_2\text{O}_3$). *Phys Chem Chem Phys* 12:10933–10941
28. Ruzsak M, Witkowski S, Pietrzyk P, Kotarba A, Sojka Z (2011) The role of intermediate calcium aluminate phases in solid state synthesis of mayenite ($\text{Ca}_{12}\text{Al}_{14}\text{O}_{33}$). *Funct Mater Lett* 4:183–186
29. Pietrzyk P, Podolska K, Sojka Z (2011) Role of $\text{NO}^{\delta+}$ intermediates in NO reduction with propene over NiZSM-5 zeolite revealed by EPR and IR spectroscopic investigations and DFT modeling. *J Phys Chem C* 115:13008–13015
30. Pietrzyk P, Podolska K, Mazur T, Sojka Z (2011) Heterogeneous binding of dioxygen-EPR and DFT evidence for side-on nickel(II)-superoxo adduct with unprecedented magnetic structure hosted in MFI zeolite. *J Am Chem Soc* 133:19931–19943
31. Dzwigaj S, Peltre MJ, Massiani P, Davidson A, Che M, Sen T, Sivasanker S (1998) Incorporation of vanadium species in a dealuminated β zeolite. *Chem Commun* 87–88
32. Pietrzyk P, Sojka Z, Dzwigaj S, Che M (2007) Generation, identification and reactivity of paramagnetic VO_2 centers in zeolite BEA for model studies of processes involving spin pairing, electron transfer and oxygen transfer. *J Am Chem Soc* 129:14174–14175
33. Spalek T, Pietrzyk P, Sojka Z (2005) Application of genetic algorithm joint with the Powell method to nonlinear least-squares fitting of powder EPR spectra. *J Chem Inf Model* 45:18–29
34. Schreckenbach G, Ziegler T (1997) Calculation of the g-tensor of electron paramagnetic resonance spectroscopy using gauge-including atomic orbitals and density functional theory. *J Phys Chem A* 101:3388–3399
35. ADF2012, SCM, Theoretical Chemistry, Vrije Universiteit, Amsterdam, <http://www.scm.com>
36. Neese F (2007) ORCA—An ab initio, Density Functional and Semiempirical Program Package, Version 2.6-00, (Lehrstuhl für Theoretische Chemie, Bonn)
37. Pietrzyk P, Podolska K, Sojka Z (2013) In: Gilbert BC, Murphy DM, Chechik V (eds) *Electron paramagnetic resonance*. RSC Publishing, Oxford
38. Mabbs FE, Collison D (1992) *Electron paramagnetic resonance of d transition metal compounds*. Elsevier, Amsterdam
39. Ovchinnikov IV, Konstantinov VN (1978) Extra absorption peaks in EPR spectra of systems with anisotropic g-tensor and hyperfine structure in powders and glasses. *J Magn Reson* 32:179–190
40. Pilbrow JR, Lowrey MR (1980) Low-symmetry effects in electron paramagnetic resonance. *Rep Prog Phys* 43:433–495
41. Pietrzyk P, Mazur T, Sojka Z (2014) In: Bruce DW, O'Hare D, Walton RI (eds) *Local structural characterization*. Wiley, Chichester
42. Giamello E, Paganini MC, Murphy DM, Ferrari AM, Pacchioni G (1997) A combined EPR and quantum chemical approach to the structure of surface $\text{F}_s^+(\text{H})$ centers on MgO . *J Phys Chem B* 101:971–982
43. Che M, Taarit BY (1985) The paramagnetic resonance principles and fundamental parameters in powder spectra. *Adv Coll Inter Sci* 23:179–213
44. Stoll S, Schweiger A (2006) EasySpin, a comprehensive software package for spectral simulation and analysis in EPR. *J Magn Reson* 178:42–55
45. Ruzsak M, Witkowski S, Sojka Z (2007) EPR and Raman investigations into redox chemistry of nanoporous $12\text{CaO} \cdot 7\text{Al}_2\text{O}_3$ interacting with O_2 , H_2 and N_2O . *Res Chem Intermed* 33:689–703
46. Hayashi K, Hirano M, Matsuishi S, Hosono H (2002) Microporous crystal $12\text{CaO} \cdot 7\text{Al}_2\text{O}_3$ encaging abundant O^- radicals. *J Am Chem Soc* 124:738–739
47. Gonchar A, Risse T, Freund H-J, Giordano L, Valentin CD, Pacchioni G (2011) Activation of oxygen on MgO : O_2^- radical ion formation on thin, metal-supported $\text{MgO}(001)$ films. *Angew Chem Int Ed* 50:2635–2638
48. Novara C, Alfayate A, Berlier G, Maurelli S, Chiesa M (2013) The interaction of H_2O_2 with TiAlPO-5 molecular sieves: probing the catalytic potential of framework substituted Ti ions. *Phys Chem Chem Phys* 15:11099–11105
49. Che M, Sojka Z (2001) Electron transfer processes at the surface of $\text{MoO}_x/\text{SiO}_2$ catalysts. *Top Catal* 15:211–217
50. Pietrzyk P, Mazur T, Podolska K, Chiesa M, Sojka Z (2013) Intimate binding mechanism and structure of trigonal nickel(I) monocarbonyl adducts in ZSM-5 zeolite-spectroscopic continuous wave EPR, HYSCORE and IR studies refined with DFT quantification of disentangled electron and spin density redistributions. *J Am Chem Soc* 135:15467–15478
51. Chiesa M, Giamello E, Paganini MC, Sojka Z, Murphy DM (2002) Continuous wave electron paramagnetic resonance investigation of hyperfine structure of $^{17}\text{O}_2^-$ adsorbed on the MgO surface. *J Chem Phys* 116:4266–4274

52. Giamello E, Sojka Z, Che M, Zecchina A (1986) Spectroscopic study of superoxide species formed by low-temperature adsorption of oxygen onto CoO-MgO solid solutions: an example of synthetic heterogeneous oxygen carriers. *J Phys Chem* 90:6084–6091
53. Sojka Z, Giamello E, Che M, Zecchina A, Dyrek K (1988) Electronic structure and orientation of dioxygen species on the surface of CoO-MgO solid solution. *J Phys Chem* 92:1541–1547
54. Pietrzyk P, Sojka Z, Giamello E (2012) In: Che M, Vedrine J (eds) *Characterization of solid materials and heterogeneous catalysts: from structure to surface reactivity*. Wiley, Weinheim
55. Känzig W, Cohen MH (1959) Paramagnetic resonance of oxygen in alkali halides. *Phys Rev Lett* 3:509–510
56. Chiesa M, Paganini MC, Giamello E, Murphy DM (1997) Surface color centers on calcium oxide: an electron paramagnetic resonance investigation. *Langmuir* 13:5306–5315
57. Schreckenbach G, Ziegler T (1995) Calculation of NMR shielding tensors using gauge-including atomic orbitals and modern density functional theory. *J Phys Chem* 99:606–611
58. Pietrzyk P, Podolska K, Sojka Z (2008) DFT analysis of g and ^{13}C hyperfine coupling tensors for model $\text{NiI}(\text{CO})_n\text{L}_m$ ($n = 1\text{--}4$, $\text{L} = \text{H}_2\text{O}$, OH^-) complexes epitomizing surface nickel(I) carbonyls. *J Phys Chem A* 112:12208–12219
59. Fukuzumi S, Ohkubo K (2000) Quantitative evaluation of Lewis acidity of metal ions derived from the g values of ESR spectra of superoxide: metal ion complexes in relation to the promoting effects in electron transfer reactions. *Chem Eur J* 6:4532–4535
60. Lindsay DM, Herschbach DR (1974) ESR of matrix isolated alkali superoxide. *Chem Phys Lett* 25:175–181
61. Napoli F, Chiesa M, Giamello E, Preda G, Di Valentin C, Pacchioni G (2010) Formation of superoxo species by interaction of O_2 with Na atoms deposited on MgO Powders: a combined continuous-wave EPR (CW-EPR), hyperfine sublevel correlation (HYSCORE) and DFT study. *Chem Eur J* 16:6776–6785
62. Chiesa M, Paganini MC, Giamello E, Murphy DM (2001) Partial ionization of cesium atoms at point defects over polycrystalline magnesium oxide. *J Phys Chem B* 105:10457–10460
63. Giamello E, Murphy D, Garrone E, Zecchina A (1993) Formation of superoxide ions upon oxygen adsorption on magnesium-doped magnesium oxide: an EPR investigation. *Spectrochim Acta Part A* 49:1323–1330
64. Weltner W Jr (1983) *Magnetic atoms and molecules*. Dover Publications, New York